CrossMark

electronic reprint

Acta Crystallographica Section B
Structural Science,
Crystal Engineering
and Materials

ISSN 2052-5206

Average structures of the disordered β-phase of Pigment Red 170: a single-crystal X-ray diffraction study

Rangana Warshamanage, Anthony Linden, Martin U. Schmidt and Hans-Beat Bürgi

Acta Cryst. (2014). B**70**, 283–295

Copyright © International Union of Crystallography

Author(s) of this paper may load this reprint on their own web site or institutional repository provided that this cover page is retained. Republication of this article or its storage in electronic databases other than as specified above is not permitted without prior permission in writing from the IUCr.

For further information see http://journals.iucr.org/services/authorrights.html

Acta Crystallographica Section B: Structural Science, Crystal Engineering and Materials publishes scientific articles related to the structural science of compounds and materials in the widest sense. Knowledge of the arrangements of atoms, including their temporal variations and dependencies on temperature and pressure, is often the key to understanding physical and chemical phenomena and is crucial for the design of new materials and supramolecular devices. *Acta Crystallographica B* is the forum for the publication of such contributions. Scientific developments based on experimental studies as well as those based on theoretical approaches, including crystal-structure prediction, structure–property relations and the use of databases of crystal structures, are published.

Crystallography Journals Online is available from **journals.iucr.org**

Acta Crystallographica Section B
Structural Science, Crystal Engineering and Materials
ISSN 2052-5206

Average structures of the disordered β-phase of Pigment Red 170: a single-crystal X-ray diffraction study

Rangana Warshamanage,[a] Anthony Linden,[a]* Martin U. Schmidt[b] and Hans-Beat Bürgi[a,c]

[a]Department of Chemistry, University of Zürich, Winterthurerstrasse 190, CH-8057 Zurich, Switzerland, [b]Institute of Inorganic and Analytical Chemistry, Goethe-University, Frankfurt, Germany, and [c]Department of Chemistry and Biochemistry, University of Bern, Switzerland

Correspondence e-mail: anthony.linden@chem.uzh.ch

Received 12 July 2013
Accepted 8 January 2014

The β-phase of the industrially important Pigment Red 170 (β-P.R. 170) has a structure with severe layer stacking disorder. The single-crystal X-ray diffraction pattern consists of a difficult-to-disentangle mix of Bragg diffraction superimposed on rods of diffuse scattering which impede the estimation of accurate Bragg intensities. Two average monoclinic structure models with the same unit-cell dimensions, but different extents of disorder in the layers and different space groups seem plausible, one with the non-conventional space group setting $B2_1/g$ (No. 14, $Z' = 2$) and one in $P2_1/a$ (No. 14, $Z' = 4$). Disordered molecules related by a translation of 0.158**b** are present in all layers of the $B2_1/g$ model and in every second layer of the $P2_1/a$ model. Layer-to-layer contacts are practically the same in both models. According to order–disorder theory, both models are valid superposition structures. Structure-factor calculations show that the pattern of strong and weak Bragg reflections is very similar for the two models. R factors indicate that the $B2_1/g$ model is the most economic representation of the average structure. However, given the limitations in data processing, the $P2_1/a$ model should not be discarded and further insight sought from a detailed analysis of the experimental diffuse scattering. The difficulties encountered in this analysis raise the question of whether or not the concept of an average structure is applicable in practice to β-P.R. 170.

1. Introduction

Hydrazone pigments, formerly called ‘azo pigments’, are an important class of chemicals because of their insolubility in most solvents and their remarkable colouristic properties. They are used in various applications, *e.g.* in paints and coatings, in the textile industry, in plastics, resins and inks (Herbst & Hunger, 2004). Pigment Red 170 (P.R. 170) is a representative of this class (Fig. 1); it belongs to the Naphthol AS class (‘Naphthol AS’ = ‘Naphthol + Amid der Säure’ = naphthoic acid amide).

P.R. 170 exists in three known crystalline phases: the nanocrystalline brown α-phase emerges from the synthesis. Its crystal structure was determined by X-ray powder diffraction *via* the isotypic structure of a methylated derivative using lattice-energy minimization (Schmidt *et al.*, 2006). The molecules form a three-dimensional hydrogen-bonded network with the molecules arranged in a herringbone fashion. The α-phase is metastable and transforms into the red β-phase upon heating in water to 373 K. Single crystals of the β-phase are obtained by recrystallizing the pigment in high-boiling solvents like *N*-methylpyrrolidone at about 473 K. The β-phase is used in industry for the colouration of plastics (Herbst & Hunger, 2004). When the α-phase is heated in water under

doi:10.1107/S2052520614000407

pressure to 403 K for 3 h, it transforms into the γ-phase, which is used in industry for lacquers and coatings, and has a bright red shade. In the γ-phase, the molecules form a two-dimensional hydrogen-bond network, resulting in wave-like layers. The β-phase has a somewhat more bluish shade than the γ-phase.

In this paper, we present a single-crystal X-ray diffraction study of the β-phase of P.R. 170. The diffraction pattern is dominated by rods of strong diffuse streaks implying that the material has a layered structure with severe stacking disorder. For background information on diffuse scattering, the reader is referred to Welberry (2004). In essence, diffuse scattering arises through a breakdown of periodicity in a crystal structure. This may be a result of thermal, occupational, compositional, orientational or translational disorder. In molecular crystals, the molecules often break crystal symmetry by assuming different orientations or conformations in different unit cells. In the case of instantaneous disorder, the diffuse scattering is called ‘thermal diffuse scattering’, while permanent breakdown of order leads to ‘static disorder scattering’. In a routine crystal structure determination, one generally only considers the Bragg scattering, regardless of whether or not the diffuse scattering intensity is significant. In cases of severe disorder, the total diffuse scattering intensity may be comparable in magnitude with the total Bragg scattering and should, therefore, not be neglected. Layer stacking disorder can arise when molecules in the crystal are arranged with excellent periodicity within layers, but the adjacent layers are positioned such that there is no periodicity in the stacking direction. This manifests itself in the diffraction pattern as rods of diffuse scattering which run parallel to the direction in which the periodicity is absent. Some examples of the description and interpretation of diffuse scattering in the case of layer stacking disorder are given in Welberry & Goossens (2008), Krüger *et al.* (2011), Gardon *et al.* (2003) and Bürgi *et al.* (2005).

This report will describe the observed single-crystal diffraction pattern of β-P.R. 170, the challenges faced in distinguishing Bragg reflections from diffuse scattering when these features intersect and the derivation of some disordered models to describe the average structure, based on the Bragg reflections only. As it is very difficult to distinguish Bragg reflections from diffuse scattering signals, we are at the limit of what can be done with standard software. Consequently, ambiguities remain which require the discussion to be more detailed than usual. The companion paper immediately following this one describes and derives the local structure and layer stacking probabilities from extensive lattice-energy minimizations (Teteruk *et al.*, 2014). Work is in progress on the modelling of the local structure from the experimental diffuse scattering data using Monte Carlo simulations and genetic algorithms.

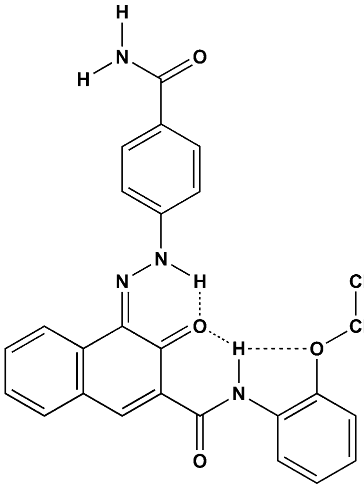

Figure 1
Pigment Red 170, $C_{26}H_{22}N_4O_4$.

2. Experimental

2.1. Crystallization

Single crystals of the β-phase of P.R. 170 were obtained by dissolving a mixture of 1.0 g of the α-phase of P.R. 170 and 0.2 g of the β-phase of P.R. 170 in 15 ml of boiling *N*-methyl-2-pyrrolidone at 476 K, and subsequent slow cooling to room temperature. The crystals were isolated by filtration, washed with ethanol and dried. Rapid cooling yields the same polymorph, but as smaller crystals.

2.2. X-ray data collection

A β-P.R. 170 single crystal, brilliant red in colour, with approximate dimensions 0.30 × 0.15 × 0.15 mm was mounted on a loop and used for the data collection. Three-dimensional X-ray scattering data were collected at 100 K with the KM6 diffractometer of beamline BM01A at the Swiss–Norwegian Beamline of the ESRF. Two datasets were collected: one at λ = 0.7083 Å using an Oxford Diffraction Onyx CCD detector at a crystal–detector distance of 100 mm, ω-scan slicing of 1° per frame and up to 0.54 Å resolution. The exposure time per frame was chosen to provide an approximately constant dose and varied between 1 and 8 s. The other dataset was collected at λ = 0.6973 Å using an Agilent Technologies Titan CCD detector at a crystal–detector distance of 120 mm, ω-scan slicing of 0.5° per frame, exposure time per frame of 1 s and up to 0.81 Å resolution. All processing of the data was carried out using *CrysAlisPro* (Agilent Technologies, 2012), including the generation of reciprocal lattice layer images and the intensity profiles shown in Figs. 2–4.

The details of the diffraction pattern were scrutinized using the second dataset with finer slicing (§3). The first dataset with its much higher resolution was used for modelling the average structure (§4).

3. Observations

3.1. Description of the diffraction pattern

The diffraction pattern appears to consist of Bragg reflections and rods of strong diffuse scattering. The latter run in one direction only and pass through Bragg reflections, *i.e.* there are no rows of Bragg reflections that are not coincident

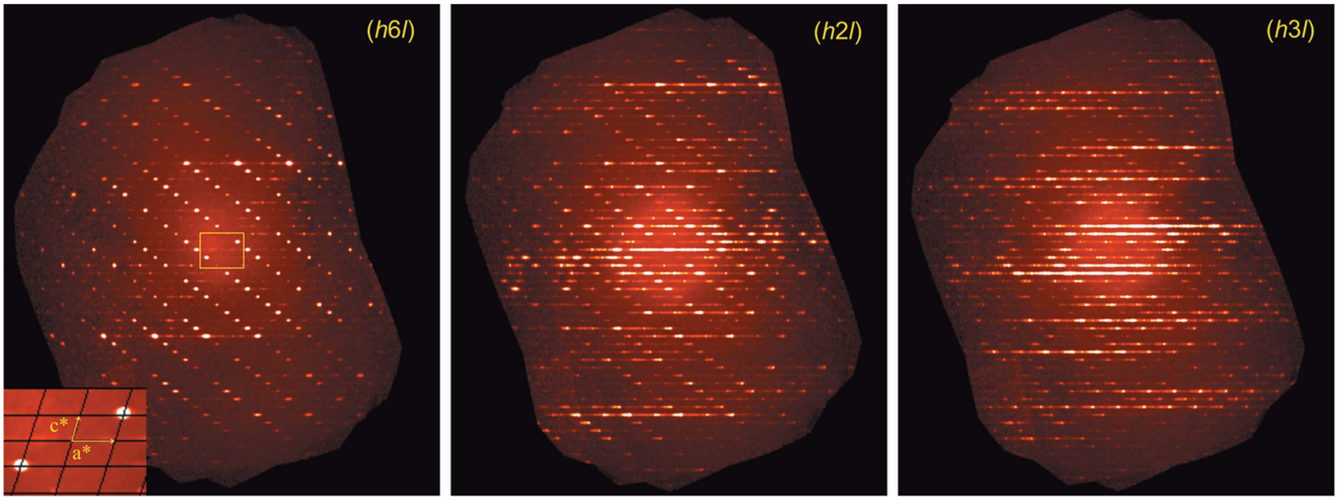

(*a*) (*b*) (*c*)

Figure 2
Reconstructions of reciprocal lattice layers showing (*a*) a type *A* layer (*h*6*l*: reciprocal unit cell axes are shown in the inset); (*b*) a type *B* layer (*h*2*l*); (*c*) a type *C* layer (*h*3*l*). Views of additional layers can be found in Fig. S1 of the supporting material.

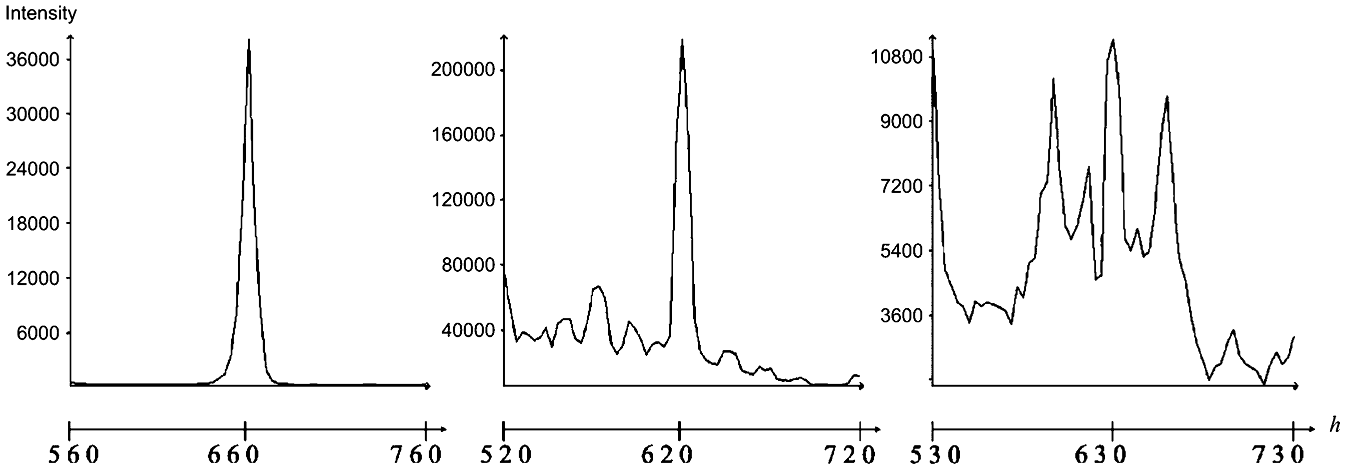

(*a*) (*b*) (*c*)

Figure 3
Representative intensity profiles along increasing *h*. (*a*) The type *A* reflection 660; (*b*) the type *B* reflection 620; (*c*) the type *C* reflection 630.

with at least some diffuse scattering. The diffuse features that can readily and clearly be seen are described in §3.1.1, while those which need more detailed analysis are described in §3.1.2.

The Laue symmetry of the total diffraction pattern is $2/m$ and is conveniently described in a monoclinic unit cell with parameters a = 14.4285 (5), b = 24.7715 (5), c = 24.9914 (8) Å, β = 109.738 (3)° and diffuse streaks running parallel to **a***. The derivation of possible unit cells from the Bragg reflections, and the difficulties associated therewith, will be described in detail in §3.2.1.

3.1.1. Coarse features. Comparison of the reciprocal lattice layers *hnl* (n = 0–23), *hk*0 and 0*kl* clearly show that the rods of diffuse scattering are always parallel to **a***. With increasing n, the diffuse features in successive *hnl* layers cycle through a pattern with a repeat of 6.33**b***. A cycle starts with a layer showing what looks like sharp Bragg reflections (*e.g.* *h*0*l*) and quite weak and short diffuse lines. It progressively moves through weakening Bragg and strengthening diffuse features to a maximum of strong diffuse rods with barely discernable Bragg reflections (*e.g.* *h*3*l*), then the trend reverses and returns to the sharp Bragg/weak diffuse pattern (*e.g.* *h*6*l*) before the cycle starts again. The layers can be divided qualitatively into three basic classes depending on where in the cycle each layer is. The *Bragg-like layers* (type *A*) clearly show the Bragg lattice with minimal diffuse features [*e.g.* *h*0*l*, *h*1*l*, *h*6*l*, *h*7*l*, *h*12*l*, *h*13*l*, *h*19*l* and *h*20*l*; see Fig. 2(*a*) and the supporting information[1]]. On the *mixed-type layers* (type *B*), Bragg-like reflections can still be seen throughout the reciprocal layer; however, the diffuse rods are more intense and give the Bragg

---

[1] Supplementary data for this paper are available from the IUCr electronic archives (Reference: OG5065). Services for accessing these data are described at the back of the journal.

reflections the appearance of being elongated along **a***, with the reflections at higher angles tending to be elongated asymmetrically. Typical examples are *h*2*l* (Fig. 2*b*), *h*5*l*, *h*8*l*, *h*11*l*, *h*14*l*, *h*15*l*, *h*17*l* and *h*18*l*. Bragg reflections on the *layers dominated by diffuse scattering* [type *C*, *e.g. h*3*l* (Fig. 2*c*), *h*4*l*, *h*9*l*, *h*10*l*, *h*16*l and h*17*l*] are superimposed by strong diffuse streaks. Identifying the Bragg reflections is difficult.

In type *A* and type *B* layers the majority of strong reflections fall onto rows which run parallel to (10$\bar{1}$) with a spacing in the **a*** direction of 4**a***. In the range $-2 \le n \le 2$, these reflection rows cut through the **a*** axis at $h = 4m$ (*m* is an integer) in *hnl* layers with *n* even (... −2, 0, 2 ...), while they cut **a*** at $h = 4m + 2$ in layers with *n* odd (... −1, 1 ...). In the range $5 \le n \le 8$ the situation is opposite: the case $h = 4m$ is associated with *n* odd, the one with $h = 4m + 2$ is associated with *n* even. The changeover takes place at the type *C* layers, where these rows cannot be discerned easily. This pattern also repeats with the periodicity of $n \simeq 6.33$.

3.1.2. Fine features. The intensity profiles along **a*** in the neighbourhood of the Bragg reflections differ in the three types of layers. As shown in Fig. 3, which is representative of reflections with low *l*, the *A*-type reflection 660 appears to be symmetric, relatively sharp and hardly affected by diffuse scattering. The *B*-type reflection 620 is comparably sharp, but sits on a structured diffuse signal. Separation of the Bragg signals from the diffuse signals and the extraction of accurate *B*-type Bragg intensities are difficult.

The *C*-type reflection 630 appears broader than the *A*- and *B*-type reflections and is surrounded by signals of similar magnitude. It should be considered as a superposition of a Bragg reflection and a comparatively intense diffuse signal, as is indicated by the diffuse maxima at non-integer *h* values, which are irregularly spaced and thus probably not supercell reflections. In this situation, determination of a reliable Bragg intensity appears hopeless. Fig. 4 depicts a similar analysis of reflections with high *l* where the *B*- and *C*-type high-angle reflections are elongated asymmetrically along the diffuse lines in only one direction; the features of the lines chosen in Fig. 4 always extend to the side of more positive *h*, the direction of higher diffraction angles (Figs. 4*b* and *c*). The maxima of the profiles appear slightly displaced from integer reciprocal lattice positions. It is difficult to say whether this

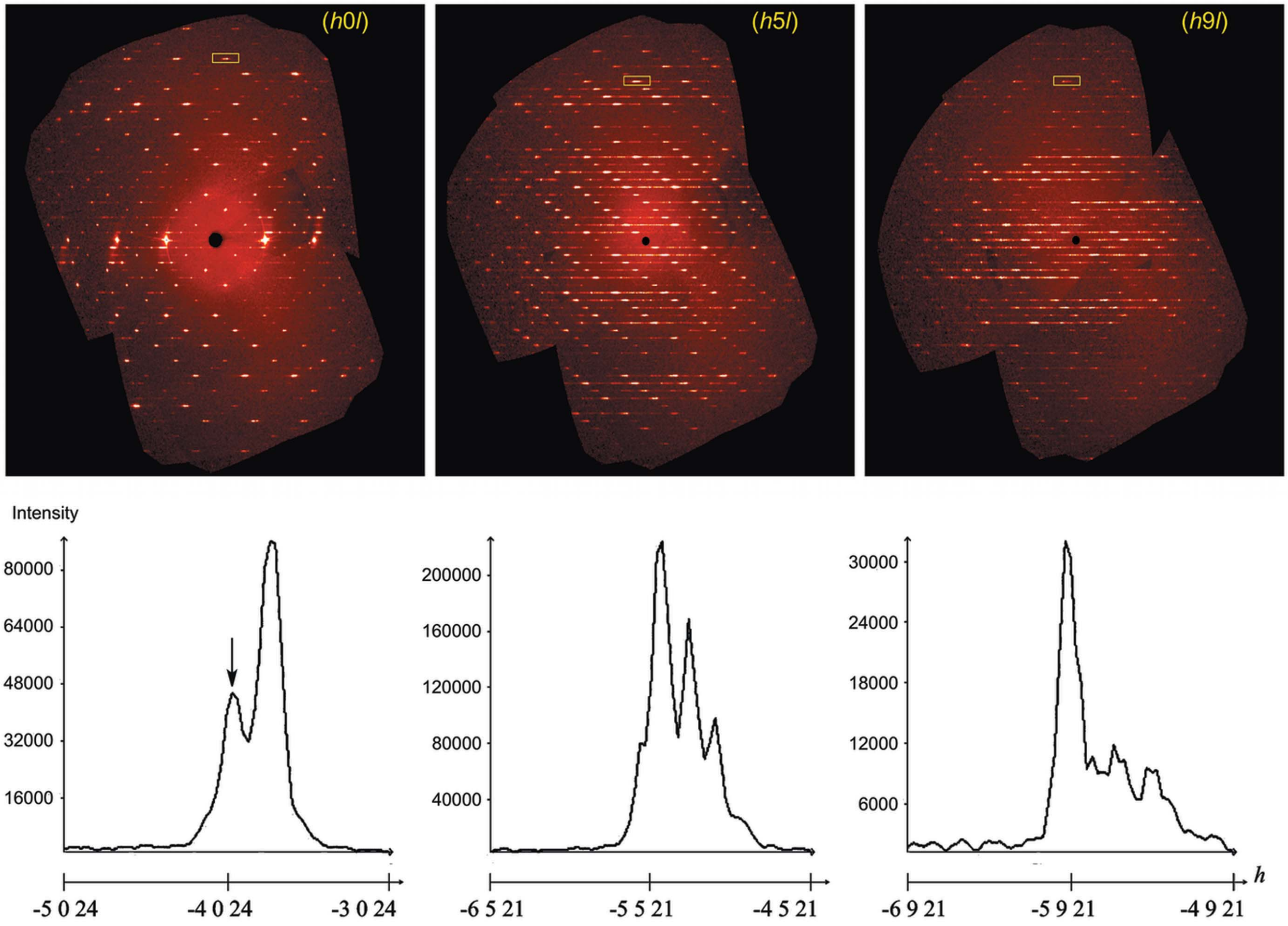

(*a*) (*b*) (*c*)

Figure 4
Reconstructions of different types of reciprocal lattice layers and representative intensity profiles along increasing *h* of the region taken from the yellow rectangles. (*a*) *Type A Bragg-like* layer *h*0*l* with a profile around −4 0 24 (the position of the Bragg peak is arrowed); (*b*) *mixed-type B* layer *h*5*l* with a profile around −5 5 21; (*c*) *diffuse-type C* layer *h*9*l* with a profile around −5 9 21.

Table 1
Lattice constants of the unit cells UC1, UC2, TC1 and TC2 after constraining to monoclinic symmetry.

UC1 and UC2 correspond with the standard settings as produced by the software. TC1 and TC2 are the transformed versions of UC1 and UC2 with the transformation matrices given in Fig. 5.

Cell	*a*, *b*, *c* (Å)	β (°)	Space group
UC1	12.1367 (2), 24.7715 (5), 14.4285 (5)	104.283 (3)	$P2_1/n$
UC2	14.4270 (4), 24.7749 (3), 24.2774 (4)	104.213 (2)	$P2_1/a$
TC1	14.4285 (5), 24.7715 (5), 24.9914 (8)	109.738 (3)	$B2_1/g$
TC2	14.4270 (4), 24.7749 (3), 25.0108 (6)	109.786(2)	$P2_1/a$

feature is intrinsic to this diffraction pattern or due to the orientation matrix being biased to some extent by the diffuse signals. Again, the Bragg signals are affected by the superimposed diffuse scattering.

Even in the *A*-type layers, higher-angle Bragg reflections are poorly resolved. Unlike *B*- and *C*-type higher-angle reflections, the Bragg intensity is sometimes smaller than the neighbouring diffuse maximum (Fig. 4*a*). It might be argued that such split peak features are the result of a poorly determined orientation matrix or a crystal that is not single. However, all attempts to find a second Bragg lattice using the *CrysAlisPro* (Agilent Technologies, 2012) multi-crystal/twin-indexing routines were unsuccessful. Some of the features described in this section have also been identified in the raw data frames. Together these observations confirm that the observed diffraction features are most likely a signature of the disorder inherent to this material.

3.2. Interpretation of the diffraction pattern

3.2.1. Indexing and unit-cell determination. Since the Bragg reflection profiles are affected by rods of diffuse scattering, unit-cell determination, reflection indexing and determination of Bragg reflection intensities are non-trivial. In the absence of unaffected or minimally affected Bragg reflections at high scattering angles, it is very difficult to determine an unbiased and unambiguous orientation matrix. The critical question when determining the unit-cell parameters and analysing for systematic absence conditions is whether or not any intensity seen at the position of a potential Bragg reflection is indeed Bragg intensity, or only intensity resulting from diffuse scattering passing through the Bragg position. To deal with this difficulty, a series of unit-cell determinations was carried out. In the first step of each attempt, a peak list was generated by choosing a minimum intensity threshold which eliminated as many diffuse signals as possible. However, it is clear from the diffraction pattern (see Figs. 2 and 4) that the intensities of some diffuse signals are similar in magnitude to Bragg intensities. Therefore, the inclusion of some diffuse signals in the peak list is unavoidable and leads to an ambiguity in the determination of the Bravais lattice and other systematic absences.

Two possible unit cells were found (Table 1). This ambiguity and the fact that a different plausible model could be established for the average structure using each of these unit cells (see §§4 and 5) provided no basis for choosing a unique unit cell and model, and so both had to be pursued. Regardless of the threshold value, monoclinic unit cell one (UC1) was found very frequently, while unit cell two (UC2) was found only with lower thresholds. UC2 can be derived from UC1 by doubling the **a** axis and interchanging the **a** and **c** axes. In these standard unit-cell settings, the diffuse streaks are not parallel to any of the reciprocal cell axes. In order to simplify simulations of the diffuse scattering and the description of the disordered layer stacking, it is more convenient to choose unit cells which have a direct axis parallel to the stacking direction and the corresponding reciprocal axis parallel to the direction of the diffuse streaks. Therefore, for all subsequent work, the unit cells in Table 1 were transformed to these more convenient non-standard settings (TC1 and TC2) by using the matrix operations [0 0 −1 / 0 1 0 / 2 0 1] and [−1 0 0 / 0 −1 0 / 1 0 1] on UC1 and UC2, respectively, as shown in Fig. 5. The transformed unit-cell parameters are given in Table 1.

3.2.2. Extraction of the Bragg intensities. As described in detail in §3.1, the Bragg reflections are superimposed to varying degrees by the diffuse signals implying great difficulties in the extraction of reliable Bragg intensities. One way to cope with this problem to some extent is to fit the reflection profiles to a calculated profile. A reflection profile shape is given by the three mosaic parameters (*e*1, *e*2 and *e*3), where *e*3 is defined to be perpendicular to the detector plane, whereas *e*1 and *e*2 lie in the detector plane. For a normal

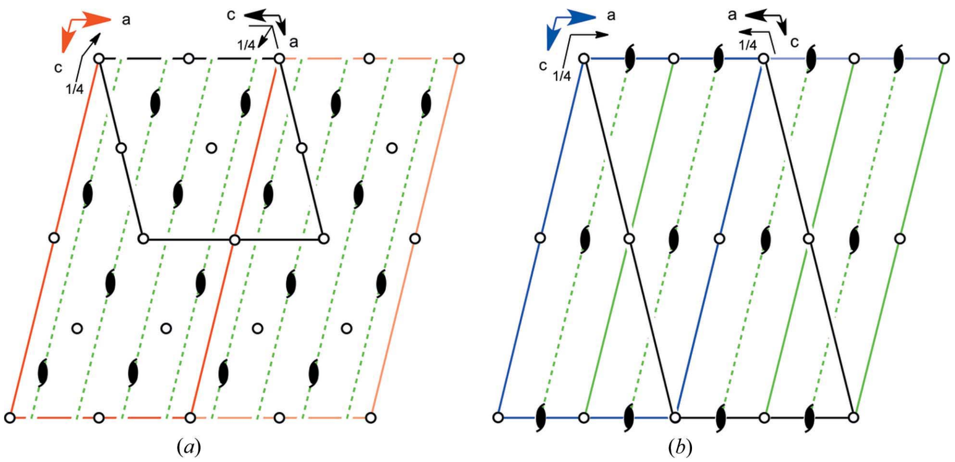

(*a*) (*b*)

Figure 5
(*a*) Transformation of UC1 (black) to TC1 (red); transformation matrix, *Tx* = [0 0 −1 / 0 1 0 / 2 0 1]. (*b*) Transformation of UC2 (black) to TC2 (blue); transformation matrix, *Tx* = [−1 0 0 / 0 −1 0 / 1 0 1]. Solid and dashed green lines indicate the positions of molecular layers parallel to the **bc** plane in all unit cells. TC1 and TC2 have the same metric parameters, but the structural models in them are quite different (see §4).

ordered crystal, $e1$ and $e2$ are usually a few tenths of a degree, while $e3$ depends mostly on the slicing angle. In the current study, $e2$ tends to be smaller than the $e1$ and $e3$ values, and shows a smaller standard deviation. The $e3$ value varies greatly and may be as large as 2.6°, as expected from the reflection profiles in Fig. 4. The $e1$ values also vary greatly. This unusual behaviour is a consequence of the strong diffuse streaks passing through the Bragg reflections. Using one common fitting function will therefore not suffice to suitably represent the majority of reflections. However, the software available to us does not have sufficient flexibility to circumvent this problem.

Mask size is an important parameter in the extraction of intensities. It determines the area on the detector integrated for each reflection. With the current data, if a large mask size is chosen, then a part of the diffuse streak near the Bragg reflection is also integrated leading to an overestimated Bragg intensity. In fact, regardless of mask size, if some diffuse intensity lies directly under the Bragg peak position, the intensity will be overestimated. On the other hand, if a small mask size is chosen, or the diffuse signal extends well away from the Bragg peak position, the background may include a significant amount of diffuse scattering and is overestimated, thereby leading to a reflection intensity that is too low. The extent to which this affects each reflection is highly variable. Therefore, an optimal mask size cannot readily be derived in the present case. A series of integrations was carried out using different mask sizes and for each case $R_{\rm int}$ was calculated. It was finally decided that the best mask size for the purpose was that which gives the lowest $R_{\rm int}$ and this mask size was the program default. However, it is important to keep in mind that this mask size represents the best one can do given the diffraction properties of the sample and the limitations of the software. In the final step of the data extraction, an empirical absorption correction was applied using the spherical harmonics procedure in *CrysAlisPro* and the frames were scaled to check whether the crystal has been centred properly in the synchrotron beam during the measurement. No anomalies were detected in the scaling output.

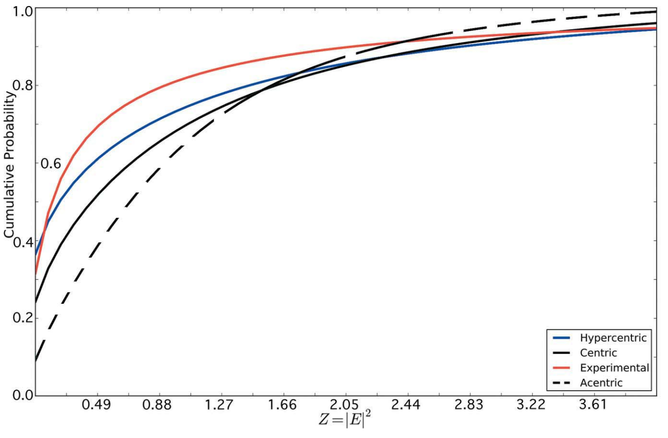

Figure 6
Cumulative probability distribution of E^2 in TC1 compared with several theoretical distributions.

3.2.3. Space-group determination

The integrated reflection intensities in each of the transformed unit cells were used for all subsequent work. Statistical analyses of intensities and space-group determination were carried out using the program *WinGX* (Farrugia, 1999). A Wilson plot and cumulative probability distribution (CPD) curves were constructed first. CPD curves are a rough, but often a good indication of the presence or absence of a centre of symmetry. In the current study, the experimental probability distribution curve does not match any of the three idealized curves, as shown in Fig. 6. It is significantly above the hypercentric distribution suggesting the presence of non-crystallographic as well as crystallographic inversion symmetry (see §5). However, this result has to be treated cautiously, given the questionable quality of the Bragg intensities.

The extinction conditions observed for the reflections in UC1 and UC2 lead to the space groups $P2_1/n$ and $P2_1/a$, respectively. After the unit-cell transformation of UC1 to TC1, the extinction conditions for the general reflections in TC1 necessarily indicate a B-centred lattice; those for the axial reflections $0k0$ indicate the presence of a 2_1 axis parallel to $\mathbf{b}$, while the zonal reflection conditions for the $h0l$ layer show the presence of an unconventional glide operation perpendicular to $\mathbf{b}$ with glide component $(\mathbf{a} - \mathbf{c})/4$. In the following, this operation is depicted by the general glide symbol g (Fischer & Koch, 1992). Therefore, the space group in TC1 was deduced to be $B2_1/g$, a non-standard, B-centred variant of $P2_1/c$, with $Z = 16$, $Z' = 2$. The list of symmetry operations defining this space group are given in Table 2. Note, however, that about 4% of the reflections that should be systematically absent under the g-glide operation ($h0l$, $h - l = 4n \pm 1$) have significant intensities. An analogous analysis of reflections for the transformed unit cell TC2 resulted in space group $P2_1/a$, $Z = 16$, $Z' = 4$. Here, as much as ~10% of the reflections that

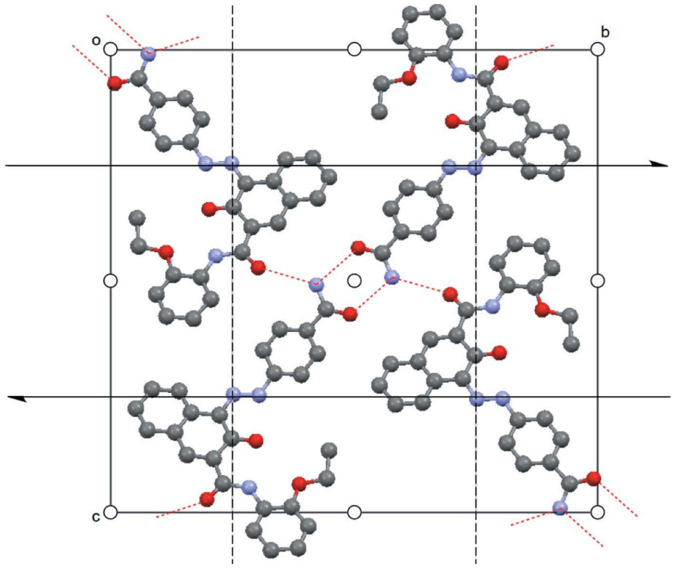

Figure 7
Idealized layer building block of P.R. 170 showing $p12_1/c1$ symmetry. Intermolecular hydrogen bonds are shown as red dashed lines.

Table 2
Crystallographic data for both models.

	Model 1	Model 2
Crystal data		
Chemical formula	$C_{26}H_{22}N_4O_4$	$C_{26}H_{22}N_4O_4$
M_r	454.48	454.48
Crystal system, space group	Monoclinic, $B2_1/g$	Monoclinic, $P2_1/a$
Temperature (K)	100	100
a, b, c (Å)	14.4285 (5), 24.7715 (5), 24.9914 (8)	14.4270 (4), 24.7749 (3), 25.0108 (6)
β (°)	109.738 (3)	109.786 (2)
V (Å^3)	8407.5 (4)	8411.8 (3)
Z, Z'	16, 2	16, 4
Radiation type	Synchrotron, λ = 0.7083 Å	Synchrotron, λ = 0.7083 Å
μ (mm^{-1})	0.10	0.10
Crystal size (mm)	0.30 × 0.15 × 0.15	0.30 × 0.15 × 0.15
Data collection		
Diffractometer	KM6 SNBL, Onyx CCD	KM6 SNBL, Onyx CCD
Absorption correction	Multi-scan (Agilent Technologies, 2012)	Multi-scan (Agilent Technologies, 2012)
$T_{\min}, T_{\max}$	0.586, 1.000	0.641, 1.000
No. of measured, independent and observed [$I > 2\sigma(I)$] reflections	201 947, 27 617, 19 694	405 722, 55 249, 28 314
$R_{\rm int}$	0.070	0.085
Scan slicing (°) per frame	1	1
Equivalent positions	$x, y, z; \frac{1}{2}+x, y, \frac{1}{2}+z;$ $\frac{3}{4}+x, \frac{1}{2}-y, \frac{1}{4}+z;$ $\frac{1}{4}+x, \frac{1}{2}-y, \frac{3}{4}+z; -x, -y, -z;$ $\frac{1}{2}-x, -y, \frac{1}{2}-z;$ $\frac{1}{4}-x, \frac{1}{2}+y, \frac{3}{4}-z;$ $\frac{3}{4}-x, \frac{1}{2}+y, \frac{1}{4}-z$	$x, y, z; \frac{1}{2}-x, \frac{1}{2}+y, -z;$ $\frac{1}{2}+x, \frac{1}{2}-y, z; -x, -y, -z$
Refinement		
R_1 [$F^2 > 2\sigma(F^2)$], $wR(F^2)$, S	0.118, 0.361, 1.40	0.186, 0.589, 2.03
Occupation [major, minor]	0.9294 (7), 0.0706 (7)	0.6478 (7), 0.3522 (7)
No. of reflections	27 617	55 249
No. of parameters	822	1435
No. of restraints	528	1320
$\Delta\rho_{\max}$, $\Delta\rho_{\min}$, rmsd (e Å^{-3})	1.77, −0.67, 0.18	1.20, −1.90, 0.15

should be systematically absent under the *a*-glide condition have significant intensities. As indicated in §3.2.1, these systematic absence violations could be real and thus be an indication that the space-group symmetries are questionable, or they could be an artefact of diffuse scattering signals passing through the Bragg reflection positions. With the tools available, it is difficult, if not impossible, to distinguish these alternatives.

4. Attempts at structure solution and refinement

All attempts at structure solution showed the layered motif in Fig. 7 to be the building unit of the β-P.R. 170 crystal structure. This motif is also found in the γ-polymorphic form (Schmidt *et al.*, 2006). Its layer symmetry is approximately $p12_1/c1$, which is an alternative setting of layer group #17 (Kopský & Litvin, 2010). Depending on the model (see below), some of these symmetry operations become crystallographic, the rest are non-crystallographic.

4.1. Model 1

The structural model developed in the space group $B2_1/g$ will be referred to as model 1. It was found in several steps by the application of direct methods and difference Fourier syntheses (Sheldrick, 2008). The asymmetric unit (ASU) contains two nearly planar P.R. 170 molecules located in the **bc** plane at $x = \frac{1}{8}$ (Fig. 5*a*). Initially they were assumed to have full occupation (*i.e.* to be ordered). This model, which included H atoms at idealized positions, was refined using *SHELXL*97 (Sheldrick, 2008) to an R_1 of ~ 0.17. Difference–Fourier (DF) maps obtained from this model showed the first 50 difference density peaks to be significant compared to the r.m.s. deviation from the mean residual density. Almost all the largest difference density peaks could be interpreted in terms of two additional P.R. 170 molecules shifted relative to those found previously by the vector −0.158**b**. The geometry of each of the new molecules was tightly restrained to be similar to the geometry of the existing molecules (using the instruction SAME in *SHELXL*97 with a standard uncertainty of 0.005 Å). The occupancies of the new and original molecules were constrained to add to 1. After several full-matrix least-squares refinement cycles (all non-H atoms anisotropic, H atoms constrained to be isotropic and in calculated positions), R_1 improved to ~ 0.12 and the principal mean-square atomic displacement parameters (ADPs) of the major components became more reasonable, whereas those of the minor components seemed unreasonably large. The latter were then constrained to be identical with the corresponding ADPs of the major components (using the EADP instruction in *SHELXL*97). This model refined to an R_1 of 0.12 with occupancies of 0.9294 (7) and 0.0706 (7) for the major and minor components, respectively, and reasonable ADPs. The DF maps synthesized from the final model (Fig. 8) did not show any electron-density peaks that could readily be interpreted as representing the positions of additional molecules. However, this observation should be treated cautiously given the uncertain quality of the integrated intensities, as described earlier. The displacement of 0.158**b** between the major and minor positions in the layer is responsible for the periodicity of 6.33**b*** (= 1/0.158**b**) relating the *A*-, *B*- and *C*-type reciprocal lattice layers described in §3.1.1.

This model resembles the structure obtained by Christie and co-workers (Christie, 2002; Christie *et al.*, 2014). They

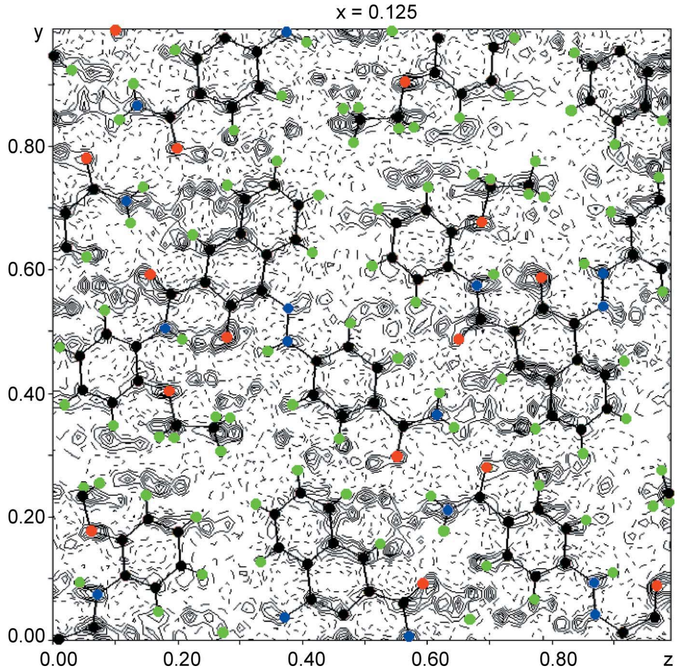

Figure 8
Difference electron density map at $x = 0.125$ of model 1 in $B2_1/g$. Positive and negative contour levels are shown by solid and dashed lines, respectively, step 0.2 e Å^{-3}. Only the molecules with the occupation factor 0.9294 (7) are shown. Minor molecules can be located by translating major molecules with the vector [0, −0.158, 0].

obtained single crystals of β-P.R. 170 by recrystallization from nitrobenzene. They measured the X-ray diffraction pattern at 160 K using a point detector. The structure was solved in the monoclinic unit cell UC1 with dimensions a = 12.156 (5), b = 24.713 (5), c = 14.464 (5) Å, β = 104.63 (5)°, space group $P2_1/n$, $Z = 8$ and $Z' = 2$. The structure of Christie corresponds to our model 1 if only the major positions are considered.

4.2. Model 2

The structural model 2 in TC2 was developed with space group $P2_1/a$, analogously to the development of model 1. There are four molecules in the ASU. Two ordered molecules are located in a layer parallel to the **bc** plane at $x = 0$ (Fig. 5*b*). The other two independent molecules are located in the layer at $x = \frac{1}{4}$ parallel to the first layer and are disordered over two sites related by the vector 0.158**b**. The disorder is similar to that in model 1, although this time the major and minor components have occupancies of 0.6478 (7) and 0.3522 (7), respectively. The refinement was carried out in an analogous fashion to that for model 1, including the use of geometric restraints and ADP constraints. At convergence, R_1 was 0.19.

DF maps from the ordered layer in this model showed difference density peaks greater than 2 e Å^{-3}, which suggest the presence of additional molecules, thus indicating that the ordered layer might actually be disordered. All attempts to include the additional molecules in a refinement were unsuccessful. This observation and the difficulties in separating Bragg from diffuse scattering led us to question the validity of the chosen space-group symmetries and to pursue the analysis of both models further.

5. Results and discussion

5.1. Description of the average structures

The P.R. 170 molecules exhibit the usual hydrazone tautomeric form (—NH—N═C), which is also observed in all other naphthol AS pigments (Kobelt *et al.*, 1972, 1974; Whitaker, 1978; Paulus, 1982; Chang *et al.*, 2003, 2009; Schmidt *et al.*, 2006). In most textbooks, P.R. 170 and other Naphthol AS pigments are still drawn in the azo tautomeric form (—N═N—C). The H atom of the CONH moiety forms a bifurcated intramolecular hydrogen bond to the O atom of the ethoxy group and of the naphthoquinone system, as drawn in Fig. 1. The molecules are not perfectly planar. The mean deviation of the atoms from the plane is ~ 0.045**a**.

The crystal structure of β-P.R. 170 is composed of molecular layers. Within these layers, molecules interact through a network of two types of hydrogen bonds. Pairs of molecules are connected by hydrogen bonds between the $CONH_2$ groups across the layer inversion centres, as shown in Fig. 7. Additional intermolecular hydrogen bonds can be found between the second H atom of the $CONH_2$ moiety and the O atom of the CONH group in a neighbouring molecule. The centrosymmetric pairs are arranged in a close-packed pattern by two *c*-glide

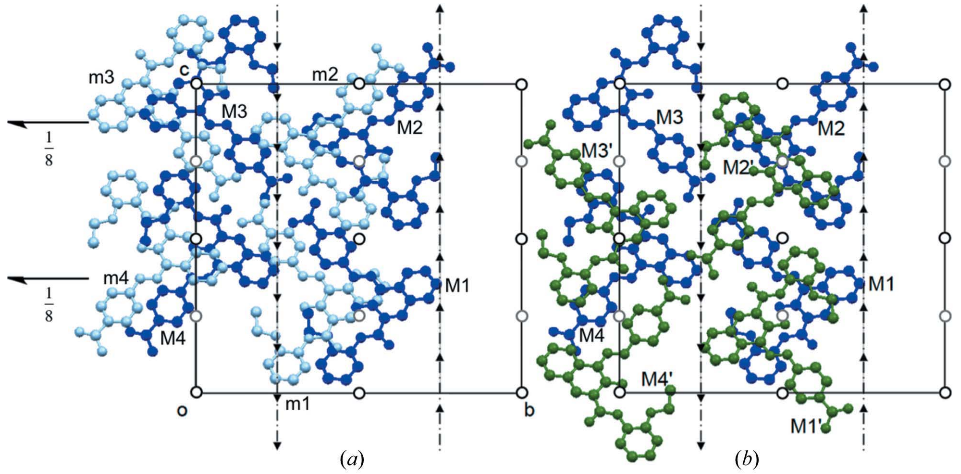

(*a*) (*b*)

Figure 9
(*a*) The molecular layer at $x = \frac{1}{8}$ in model 1 viewed down **a** showing the major (M, dark blue) and minor (m, light blue) positions related by −0.158**b**. (*b*) The two adjacent layers, at $x = \frac{1}{8}$ (blue molecules, M1–M4) and $x = \frac{3}{8}$ (green molecules, M1′– M4′) in model 1 viewed down **a**. Only the major components and the symmetry relationships between them are shown. In this figure only the first layer ($x = \frac{1}{8}$) 2_1 axes are shown. Black circles represent inversion centres at $x = 0$ and $\frac{1}{2}$ while grey circles are inversion centres at $x = \frac{1}{4}$ and $\frac{3}{4}$. The *g*-glide planes at $x, \frac{1}{4}, z$ and $x, \frac{3}{4}, z$ are also shown.

operations perpendicular to **b** and 2_1 screw rotations parallel to **b**.

The layers are parallel to the **bc** plane and stack along the **a** axis in both models, however, their placement along the stacking axis is different in the two models. As mentioned in §4, the layers show approximate $p12_1/c1$ layer symmetry. Only some of the layer symmetry operations appear as crystallographic symmetry operations in the two models, with a different subset being crystallographic in each case, as described in the next two subsections.

5.1.1. Model 1. In model 1, the **bc** planes at $x = \frac{1}{8}, \frac{3}{8}, \frac{5}{8}$ *etc.* are occupied with a superposition of two geometrically very similar molecular layers shifted relative to one another by 0.158**b**, as shown in Fig. 9(*a*), and with major and minor occupations of $M = 0.9294\ (7)$ and $m = 0.0706\ (7)$, respectively. The space group $B2_1/g$ (Table 2) implies that these layers are symmetry equivalent.

5.1.2. Model 2. In model 2, the layer stacks are built from two symmetry-independent molecular layers. One type of layer is located at $x = 0$ and $\frac{1}{2}$, while the other independent type is found at $x = \frac{1}{4}$ and $\frac{3}{4}$. The layer at $x = 0$ is ordered with molecules showing full occupation (F), whereas the layers at $x = \frac{1}{4}$ and $\frac{3}{4}$ are disordered over two positions again related by the shift vector 0.158**b**; occupation factors for the major (P) and minor (p) positions are 0.6478 (7) and 0.3522 (7), respectively. In the layer at $x = 0$ only the inversion centres of the layer group $p12_1/c1$ are crystallographic symmetries; in the layer at $x = \frac{1}{4}$ only the 2_1 operations are crystallographic (see Figs. 5*b* and 10).

5.2. Similarities and differences between Models 1 and 2

It is important to identify the similarities and differences between the two proposed models for *β*-P.R. 170 in order to understand and judge the meaning of models 1 and 2, with respect to the experimental scattering data and the structural disorder. A tool to analyse disordered arrangements of layers is provided by order–disorder (OD) theory (Dornberger-Schiff, 1956). In the present case it implies scrutinizing models 1 and 2 for local symmetries of individual layers and of pairs of layers. These symmetries are summarized in an OD groupoid symbol (§5.2.1), which characterizes all periodic and non-periodic polytypes in a single family. Groupoids are usually referred to a coordinate system with the usual translation vectors in the two periodic directions and an interlayer vector in the stacking direction, here $\mathbf{a}_0 = \mathbf{a}/4$, **b**, **c**. The local symmetries may produce non-standard systematic absences. These aspects are analysed in §5.2.2.

5.2.1. Similarities and differences in direct space, OD analysis. As mentioned before, both models are built from the same layers with approximate $p12_1/c1$ symmetry. Both models show displacive disorder to varying degrees arising purely from two disordered positions in the layers. The two positions are related by the vector 0.158**b**. Although the arrangement of the layers is different in the two average structure models, the relationships between nearest neighbour layers are the same, except in the likely rare case where adjacent layers are both composed of the minor occupied positions in model 1. Here we will only discuss the predominant relationships for model 1.

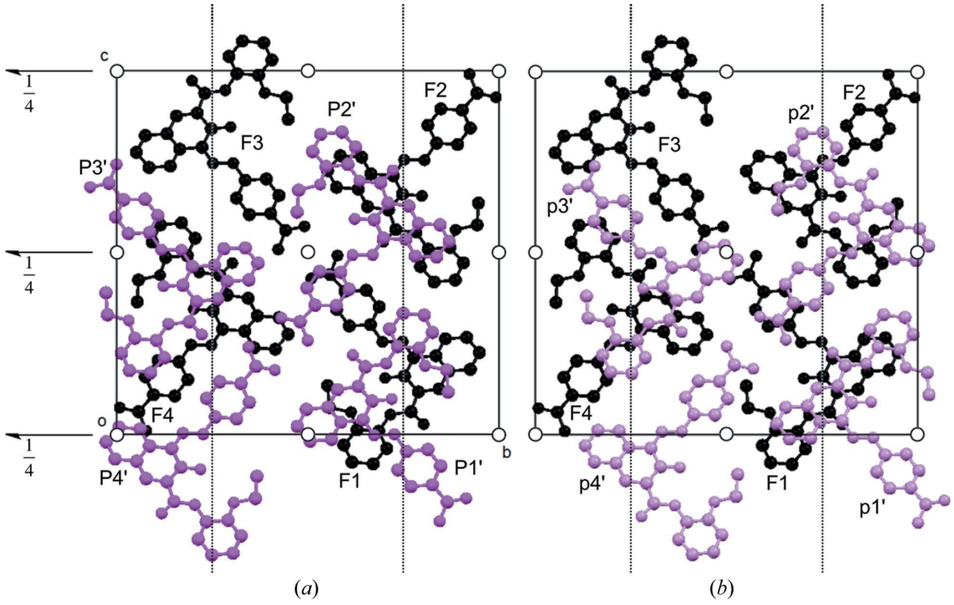

(*a*) (*b*)

Figure 10
Projection of molecular layers at $x = 0$ (ordered, black) and $\frac{1}{4}$ (disordered, magenta and violet) down **a** in model 2. (*a*) The arrangement of the major component of the layer at $x = \frac{1}{4}$ (magenta) with respect to the ordered layer. The two layers are related to each other by non-crystallographic inversion centres at $(\frac{1}{8}, \frac{1}{4} - 0.039, \frac{1}{8})$; $(\frac{1}{8}, \frac{1}{4} - 0.039, \frac{5}{8})$; $(\frac{1}{8}, \frac{3}{4} - 0.039, \frac{1}{8})$; $(\frac{1}{8}, \frac{3}{4} - 0.039, \frac{5}{8})$ and non-crystallographic *g*-glide planes at $y = 0 - 0.039$ and $\frac{1}{2} - 0.039$. (*b*) Non-crystallographic inversion centres at $(\frac{1}{8}, \frac{1}{4} + 0.039, \frac{1}{8})$; $(\frac{1}{8}, \frac{1}{4} + 0.039, \frac{5}{8})$; $(\frac{1}{8}, \frac{3}{4} + 0.039, \frac{1}{8})$; $(\frac{1}{8}, \frac{3}{4} + 0.039, \frac{5}{8})$ and non-crystallographic *g*-glide planes at $y = 0 + 0.039$ and $\frac{1}{2} + 0.039$ relate the minor component (violet) of the layer at $x = \frac{1}{4}$ to the ordered layer at $x = 0$. The crystallographic 2_1 axes located in both major and minor layers at $x = \frac{1}{4}$ are shown, while black dashed lines running parallel to the **c** axis at $y = \frac{1}{4}$ and $\frac{3}{4}$ indicate crystallographic *a*-glide planes.

Detailed relationships between the molecules in a single layer of model 1 are shown in Fig. 9(*b*). *M*1 and *M*2 (or the symmetry-related *M*4 and *M*3, respectively) constitute the asymmetric unit of the major component and, although symmetry independent, are related by the non-crystallographic glide plane perpendicular to **b** at $y = \frac{1}{2} + 0.039$ with glide component $[0, 0, \frac{1}{2}]$. Neighbouring layers are related by centres of inversion and *g*-glide operations of the $B2_1/g$ space group.

More interestingly, symmetry-independent molecules in neighbouring layers are related by non-crystallographic, local symmetry operations. A detailed analysis of these local symmetries shows that a molecule in a given layer is generally related to one or more crystallographically independent molecules of the same orientation in the adjacent layers by one of the vectors $[-\frac{1}{4}, 0.42, -\frac{1}{4}]$ (= $-\mathbf{a}/4 + 0.42\mathbf{b} - \mathbf{c}/4$), $[\frac{1}{4}, 0.42, \frac{1}{4}]$, $[\frac{1}{4}, -0.42, \frac{1}{4}]$ or $[-\frac{1}{4}, -0.42, -\frac{1}{4}]$ of length ~ 12.1 Å. As an example, $M1$ at $x = \frac{1}{8}$ is related to $M3'$ at $x = \frac{3}{8}$ by the second vector above (Fig. 11). Alternatively, the route from $M1$ to $M3'$ at $x = \frac{3}{8}$ can be given in terms of a combination of crystallographic and non-crystallographic symmetry operations. First, $M1$ is transformed to its inversion-related mate, $M1'$ (see Fig. 9*b*) in the layer at $x = \frac{3}{8}$ by the crystallographic inversion centre at $(\frac{1}{4}, \frac{1}{2}, \frac{1}{4})$ and then $M1'$ is transformed to $M3'$ by the non-crystallographic layer inversion centre at $(\frac{3}{8}, \sim 0.709, \frac{3}{8})$. The major molecule $M1$ is also related to the minor molecule m3′ of the same orientation at $x = \frac{3}{8}$ by the vector $[\frac{1}{4}, -0.42, \frac{1}{4}]$. Alternatively, $M1$ is found to be symmetry-related to $m3'$ by the crystallographic inversion symmetry operation $\bar{1}(\frac{1}{4}, \frac{1}{2}, \frac{1}{4})$ followed by the non-crystallographic layer inversion operation $\bar{1}(\frac{3}{8}, \sim 0.290, \frac{3}{8})$. The relationships discussed here for individual molecules hold for entire layers. Two neighbouring layers are also related by a twofold screw operation with a translational component of + or $-0.079\mathbf{b}$ at $(\frac{1}{4}, y, 0)$, for example. The local relationships in model 2 are the same, but because of the different space group, the separation of operations into global and local ones is different from that in model 1. A more detailed discussion of these symmetries and pictures displaying all local and global operations for models 1 and 2 are given as Figs. 4 and 5 in the following paper by Teteruk *et al.* (2014).

There is one exception to the local symmetry relationships described in the preceding paragraph. The minor components in two consecutive layers of model 1 would be related by screw operations with translational components of + or $-0.24\mathbf{b}$.

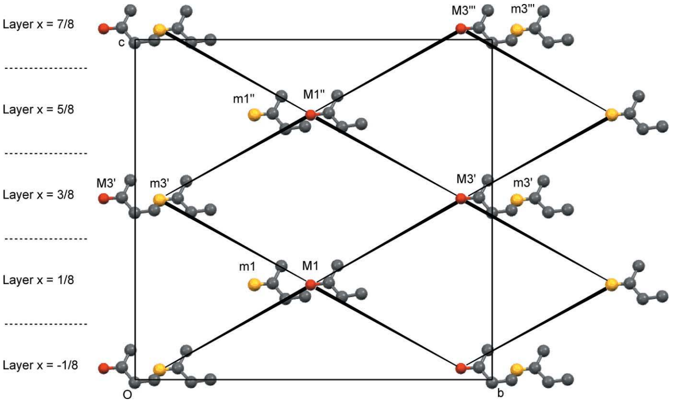

Figure 11
The arrangement of vectors relating molecules of the same orientation in model 1, as viewed down $\mathbf{a}$. Layers of P.R. 170 molecules are schematically represented by four atom fragments whose x coordinates are given at the left of the figure and represented by primed symbols. Red spheres represent the keto-oxygen atoms in molecules of the major component while yellow spheres represent the same atom in the minor components (Fig. 1). Oxygen and attached carbon atoms (grey) define the orientation of the molecule in each layer. Wedged bonds (black) connecting O atoms represent layer-to-layer vectors. Note that molecule $M3'$ is shifted by [0, 1, 0] relative to molecule $M3'$ in Fig. 9(*b*).

Summarizing in terms of groupoid language, every pair of layers in both models 1 and 2 is related by local twofold screw operations with screw component $+0.079\mathbf{b}$ or $-0.079\mathbf{b}$, symbols $2_{0.158}$ and $2_{-0.158}$, and diagonal glide operations with glide components $[\frac{1}{4}, 0, -\frac{1}{4}]$ or $[1, 0, -\frac{1}{4}]$ if referred to $\mathbf{a}_0$, $\mathbf{b}$, $\mathbf{c}$, symbol $n_{-1/2,2}$. The combination of the two operations implies local inversion operations and non-crystallographic translations, symbols $t_+ = [\frac{1}{4}, 0.421, \frac{1}{4}]$ and $t_- = [\frac{1}{4}, -0.421, \frac{1}{4}]$, or $[1, 0.421, \frac{1}{4}]$ and $[1, -0.421, \frac{1}{4}]$ if referred to $\mathbf{a}_0$, $\mathbf{b}$, $\mathbf{c}$. These operations lead to the following groupoid symbol

$$\begin{array}{cccc} P & (1) & 2_1/c & 1 \\ & \{(1) & 2_{0.158}/n_{-1/2,2} & 1\}. \end{array}$$

The local inversion and translation operations between layers mentioned above are implied by this groupoid.

The screw and inversion operations of an individual layer imply that both sides of a layer are symmetry-related and thus equivalent according to OD theory. Together with the local screw and inversion operations between layers, it follows that all interlayer contacts in both models 1 and 2 are equivalent. However, layer triples, quadruples *etc.* differ in the two models (Dornberger-Schiff & Grell-Niemann, 1961; Durovič, 2006).

The simplest way to describe the layer sequences of models 1 and 2 is in terms of t_+ and t_-. Thus, the major components of model 1 are related by the translation sequence t_+, t_-, t_+, t_- when starting with $M1$ in Fig. 11. There are then two possible alternating sequences of layers with major and minor occupation: starting from $M1$ with the translation sequence t_-, t_+, t_-, t_+, or from $M3'$ with the sequence t_+, t_-, t_+, t_-. For model 2 the layer sequence starting from an ordered layer, *e.g.* $F1$ in Fig. 12, is either t_+, t_-, t_-, t_+ when the disordered layer is always taken to be the one with major occupation sites ($P3'$) or t_-, t_+, t_+, t_-, when the disordered layer is always taken to be the one with minor occupation sites ($p3'$) (Figs. 10*b* and 12). In model

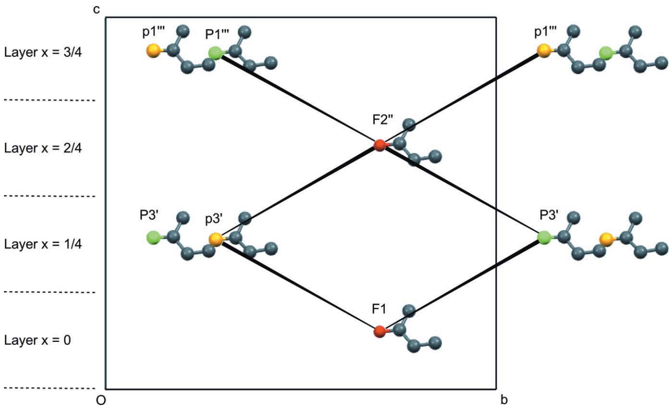

Figure 12
The arrangement of vectors relating molecules of the same orientation in model 2 as viewed down $\mathbf{a}$. Layers of P.R. 170 molecules are schematically represented by four-atom fragments whose x-coordinate is given at the left of the figure and represented by primed symbols. Red spheres indicate exocyclic O atoms in fully occupied molecular layers, while green spheres indicate the same O atoms of the major component in the disordered layer. Corresponding O atoms in the minor component are represented by yellow spheres. Wedged bonds (black) connecting O atoms represent layer-to-layer vectors.

Table 3
Coefficients of the layer form factor along (h+n, k, $-h$).

k	n	Model 1	Model 2	k	n	Model 1	Model 2
0	0	**4**	**4**	6	0	−0.18	0.02
0	1	0	0	6	1	0	0.08
0	2	0	0	6	2	**−3.99**	**3.98**
0	3	0	0	6	3	0	−0.08
0	4	**−4**	**4**	6	4	0.18	0.02
1	0	0.73	0.25	7	0	**−3.89**	**3.86**
1	1	0	−0.29	7	1	0	0.22
1	2	**−3.81**	**3.75**	7	2	−0.55	0.14
1	3	0	0.29	7	3	0	−0.22
1	4	−0.73	0.25	7	4	**3.89**	**3.86**
2	0	**−3.28**	**3.07**	8	0	−1.31	0.73
2	1	0	0.51	8	1	0	−0.46
2	2	−1.51	0.93	8	2	**3.44**	**3.27**
2	3	0	−0.51	8	3	0	0.46
2	4	**3.28**	**3.07**	8	4	1.31	0.73
3	0	−2.33	1.87	9	0	2.73	2.37
3	1	0	−0.6	9	1	0	0.59
3	2	2.53	2.13	9	2	2.13	1.63
3	3	0	0.6	9	3	0	−0.59
3	4	2.33	1.87	9	4	−2.73	2.37
4	0	1.72	1.15	10	0	2.92	2.62
4	1	0	0.54	10	1	0	−0.57
4	2	3.11	2.85	10	2	−1.92	1.38
4	3	0	−0.54	10	3	0	0.57
4	4	−1.72	1.15	10	4	−2.92	2.62
5	0	**3.7**	**3.62**	–	–	–	–
5	1	0	−0.35	–	–	–	–
5	2	−0.92	0.38	–	–	–	–
5	3	0	0.35	–	–	–	–
5	4	**−3.7**	**3.62**	–	–	–	–

1 the operation $n_{-1/2,2}$ is global. The structure formed by the layers with major occupation therefore has a maximum degree of order (MDO; Dornberger-Schiff, 1982). In model 2, none of the operations relating the layers into pairs is global; any sequence of layers includes more than one type of layer, *i.e.* layers with full and major or minor occupation, and is thus a non-MDO polytypic structure in the OD family. Note that the above sequences of layers are meant to describe the average structures in a simple way. The disordered crystal may contain other local sequences and the sequences mentioned here are not necessarily the ones occurring most frequently. A more detailed analysis of stacking sequences is given in the following paper by Teteruk *et al.* (2014).

5.2.2. Similarities and differences in reciprocal space. The displacement between the major (M or P) and the minor (m or p) components along **b** explains the features in the diffraction pattern that tend to recur with a periodicity of (1/0.158)**b*** (= 6.33**b***, see §3.1.1). The superposition of equal layers with major and minor occupation can be considered as binary disorder. In such cases, the diffuse scattering is proportional to the difference in the scattering of the disordered species (Welberry, 2004). In the present case, this difference is $2(A + B)[1 - \exp 2\pi i(0.158k)]$ [$2(A + B)$ is the layer form factor taking into account the layer symmetry $p12_1/c1$] and implies that when $0.158k$ is an integer, *e.g.* 0 or 1 for $k = 0$ or 6.33, the difference is zero and there is no diffuse scattering, as observed, at least approximately for $h0l$ and $h6l$. Conversely, the diffuse scattering is maximal if $0.158k$ is a half-integer, *e.g.* 1/2 or 3/2 for $k = 3.16$ or 9.5, again as observed for $h3l$, $h9l$ and $h10l$ (Figs. 2 and 4). The same observation also holds for higher values of k.

The local symmetries usually lead to non-crystallographic absences (Merlino, 1997). In the present case, these are fairly complex and not always perfect due to the fact that the local screw and translation components are not simple fractions of **b** (*viz.* 0.079**b** and 0.421**b**). The structure factor for model 1 can be written as

$$\begin{aligned} F(hkl) = {} & 2[\Sigma \cos 2\pi(hx_i + ky_i + lz_i) \\ & + \Sigma \cos 2\pi(hx_i - ky_i + lz_i)\cos 2\pi(k/2 + l/2)] \\ & [2M \cos 2\pi(h/8 + l/8 + 0.21k) \\ & + 2m \cos 2\pi(h/8 + l/8 - 0.63k) \\ & + 2M \cos 2\pi(3h/8 + 3l/8 - 0.21k) \\ & + 2m \cos 2\pi(3h/8 + 3l/8 + 0.63k)] \\ = {} & 2(A + B)[2M \cos 2\pi(h/8 + l/8 + 0.21k) \\ & + 2m \cos 2\pi(h/8 + l/8 - 0.63k) \\ & + 2M \cos 2\pi(3h/8 + 3l/8 - 0.21k) \\ & + 2m \cos 2\pi(3h/8 + 3l/8 + 0.63k)] \end{aligned} \tag{1}$$

corresponding to layers with occupation M at ($\frac{1}{8}$, 0.21, $\frac{1}{8}$), ($-\frac{1}{8}$, −0.21, $-\frac{1}{8}$), ($\frac{3}{8}$, −0.21, $\frac{3}{8}$) and ($-\frac{3}{8}$, 0.21, $-\frac{3}{8}$) and layers with occupation m at ($\frac{1}{8}$, −0.63, $\frac{1}{8}$), ($-\frac{1}{8}$, 0.63, $-\frac{1}{8}$), ($\frac{3}{8}$, 0.63, $\frac{3}{8}$) and ($-\frac{3}{8}$, −0.63, $-\frac{3}{8}$). The structure factor for model 2 can be written analogously as

$$\begin{aligned} F(hkl) = {} & 2(A + B)[1 + 2P \cos 2\pi(h/4 + l/4 + 0.42k) + \\ & 2p \cos 2\pi(h/4 + l/4 - 0.42k) + \cos 2\pi(h/2 + l/2)] \end{aligned} \tag{2}$$

corresponding to fully occupied layers F at (0, 0, 0) and ($\frac{1}{2}$, 0, $\frac{1}{2}$) and partially occupied layers P or p displaced by t_+ or t_-. To the extent that the atoms in a given layer are coplanar, the layer form factor $2(A + B)$ essentially consists of continuous lines at integer values of k and l which are parallel to **a***. Its absolute value decreases with increasing h due to the decrease of the atomic scattering factors, as may be gleaned from the diffuse scattering pattern.

The patterns of strong and weak lines of reflections ($h + n$, k, $-h$) in the $(10\bar{1})$ direction, described at the end of §3.1.1 and discernible from Figs. 2 and 4, follow from the modulation of the layer form factor by the terms in square brackets. Their values calculated for different values of k and n are given in Table 3. Their pattern is very similar for both models 1 and 2. The main difference is in the lines ($h + 2n + 1$, k, $-h$), which are absent in model 1 due to the B-centring and present but weak in model 2. The presence of the diffuse scattering makes it very difficult to decide whether or not the reflections ($h + 2n + 1$, k, $-h$) are present in the experimental data and thus to distinguish qualitatively between the B-centred lattice of model 1 and the primitive lattice of model 2. The similarity of the patterns of strong and weak lines ($h + 2n$, k, $-h$) precludes a distinction based on a purely qualitative comparison. The *R* factors (R_1) calculated with only the ($h + 2n$, k, $-h$) reflections, which overall are stronger than the ($h + 2n + 1$, k, $-h$) reflections, are 0.12 for model 1 and 0.18 for model 2 indicating that model 1 is probably a better explanation of the data than model 2.

Note also that in regions with distinct Bragg scattering, the intensity alternation for the lines ($h + 2n$, k, $-h$) is relatively clear-cut (*e.g.* k = 0, 1, 2, 5, 6, 7, 8), whereas in regions with strong diffuse scattering the alternation disappears (*e.g.* k = 3, 4, 9, 10).

5.2.3. Subgroup analysis. In the two preceding sections, relationships between models 1 and 2 have been discussed. One may also ask whether there are models of lower symmetry common to models 1 and 2 and providing better descriptions of the average structure. To answer this question, both models were refined in all subgroups of their respective space group down to *P*1 and introducing additional (disordered) molecules if a difference Fourier indicated them. None of these models lead to an *R* factor significantly lower than the value of ~ 0.12 found for model 1 in $B2_1/g$ (see Table S1 in the supporting information). From this observation it is concluded that model 1 is the most economic description of the Bragg data available in this study, *i.e.* the model with the highest symmetry, the smallest number of refinable parameters and the lowest *R* factor. Furthermore, from the difference Fourier syntheses calculated during the subgroup analysis, the presence of additional low-occupation disordered sites could neither be confirmed nor excluded.

6. Summary and conclusions

The scattering of the disordered β-phase of Pigment Red 170 shows a mix of what looks like Bragg diffraction superimposed on rods of strong diffuse scattering that is difficult to disentangle. As a first step in the analysis of the total scattering of the crystal and the establishment of models describing the local structure, determination of an average structure has been attempted, but doing so was far from routine. The extraction of reliable Bragg intensities from the diffraction data is severely impeded by the interference from the diffuse scattering and the available integration software does not have sufficient flexibility to circumvent this problem. Two plausible models, with different space groups, were obtained for the average structure and non-standard space group settings were chosen so as to align the rods of diffuse scattering along **a***; a convenience for comparing the models and the upcoming local structure modelling. Both models are built from the same molecular layers, which possess approximate $p12_1/c1$ symmetry and are stacked along **a***. Model 1 was established in the non-conventional space group setting $B2_1/g$ with $Z = 16$. The asymmetric unit contains two molecules which lie in the same layer and are each disordered over two positions related by a translation of 0.158**b**. Adjacent layers are related by crystallographic centres of inversion between the layers and by crystallographic *g*-glide planes, while the layers themselves have crystallographic 2_1 symmetry, but only non-crystallographic inversion symmetry. Model 2 was developed in the space group $P2_1/a$. There are four independent molecules in the asymmetric unit distributed across two independent layers. One of the layers is fully ordered and alternates with the second layer, in which the molecules are disordered over two positions again related by the 0.158**b** translation. In contrast to the $B2_1/g$ model, the ordered layers now have crystallographic inversion symmetry and non-crystallographic 2_1 symmetry, while the disordered layers possess crystallographic 2_1 axes as well as non-crystallographic inversion centres.

A detailed analysis of the local and global symmetries using OD theory showed not only that individual layers always show approximate $p12_1/c1$ symmetry, but also that all direct layer contacts are geometrically equivalent as expected for polytypes within an OD family. Salient features of the experimental diffraction pattern are explained qualitatively by both models. The agreement *R* factors calculated for model 2 with all or the subset of reflections common to models 1 and 2 were significantly higher than that from model 1 and the difference Fourier maps obtained from the ordered layer in model 2 suggested the presence within these layers of additional disordered positions for the molecules, which, however, could not be modelled successfully. The tentative conclusion from this analysis is that the model developed in $B2_1/g$ is the most appropriate representation of what we consider to be the average structure of β-P.R. 170.

The diffraction pattern of β-P.R. 170 is a fine example of a system that is right at the limit of being tractable with the tools developed for standard single-crystal structure analysis. A number of important limitations are present. Since a considerable fraction of Bragg reflections are almost completely immersed in the diffuse streaks, obtaining a reliable orientation matrix and accurate Bragg intensities is extremely difficult. Secondly, although the extent of layer disorder within each of the two models is different, they share common layer and nearest-neighbour geometries. This complicates identifying differences between the two models. Lastly, the choice of space group influences whether the various local symmetry elements in the real structure are required to be crystallographic or non-crystallographic. There is also no simple transformation between the two models. Although the model in space group $B2_1/g$ appears to be the most appropriate for describing the average structure of β-P.R. 170, the limitations and difficulties described suggest that the model in space group $P2_1/a$ or indeed other polytypes are equally probable candidates for the average structure of this sample. Thus, the average structure in a case like this is a poor representation of the true structure, so that in order to understand the structure fully, further investigations into the nature of the local structure derived from a detailed analysis of the total scattering pattern are essential. This work, which is currently underway, is expected to not only show experimentally the local stacking sequences, but also to answer the question of whether or not the concept of an average structure is applicable in practice to the β-polymorph of Pigment Red 170. The following paper (Teteruk *et al.*, 2014) discusses in detail lattice-energy minimizations and probabilities of local layer stacking sequences estimated from these calculations.

We are indebted to Dmitry Chernyshov and Phil Pattison of the Swiss Norwegian Beamlines at the ESRF for their advice and assistance during the data collection. We are most grateful to Theo Hahn for helpful suggestions concerning deriving a suitable Hermann–Mauguin space-group symbol for model 1. We also thank a referee for useful remarks, particularly with regard to OD theory. The financial support of the Swiss National Science Foundation (grant No. 200021_137866) and the University of Zürich is gratefully acknowledged.

References

Agilent Technologies (2012). *CrysAlisPro*, Version 1.171.36.20. Agilent Technologies, Yarnton, Oxfordshire, England.
Bürgi, H.-B., Hostettler, M., Birkedal, H. & Schwarzenbach, D. (2005). *Z. Kristallogr.* **220**, 1066–1075.
Chang, C.-H., Christie, R. M. & Rosair, G. M. (2003). *Acta Cryst.* C**59**, o556–o558.
Chang, C. H., Christie, R. M. & Rosair, G. M. (2009). *Dyes Pigments*, **82**, 147–155.
Christie, R. M. (2002). Presentation on *Colorchem'02, 9th International Conference on Dyes and Pigments*, 12–16 May 2002. Špindlerův Mlýn, Czech Republic.
Christie, R. M., Huang, H.-Y., Chang, C.-H., Rosair, G. M. & Powell, A. (2014). In preparation.
Dornberger-Schiff, K. (1956). *Acta Cryst.* **9**, 593–601.
Dornberger-Schiff, K. (1982). *Acta Cryst.* A**38**, 483–491.
Dornberger-Schiff, K. & Grell-Niemann, H. (1961). *Acta Cryst.* **14**, 167–177.
Durovič, S. (2006). *International Tables for Crystallography*, Vol. C, 1st online ed., edited by E. Prince, ch. 9.2.2, pp. 760–773. Chester: International Union of Crystallography.
Farrugia, L. J. (1999). *J. Appl. Cryst.* **32**, 837–838.
Fischer, W. & Koch, E. (1992). *International Tables for Crystallography*, Vol. A, 3rd ed., edited by Th. Hahn, p. 795. Dordrecht: Kluwer Academic Publishers.
Gardon, M., Pinheiro, C. B. & Chapuis, G. (2003). *Acta Cryst.* B**59**, 527–536.
Herbst, W. & Hunger, K. (2004). *Industrial Organic Pigments: Production, Properties, Applications*, 3rd ed. Weinheim: Wiley-VCH.
Kobelt, D., Paulus, E. F. & Kunstmann, W. (1972). *Acta Cryst.* B**28**, 1319–1324.
Kobelt, D., Paulus, E. F. & Kunstmann, W. (1974). *Z. Kristallogr.* **139**, 15–32.
Kopský, V. & Litvin, D. B. (2010). Editors. *International Tables for Crystallography*, Vol. E, 2nd online ed., ch. 4.1, pp. 221–391. Chester: International Union of Crystallography.
Krüger, H., Stöber, S., Welberry, T., Withers, R. & Fitz Gerald, J. (2011). *Acta Cryst.* B**67**, 476–485.
Merlino, S. (1997). *EMU Notes in Mineralogy*, Vol. 1, *Modular Aspects of Minerals*, pp 1–28. Budapest: Eötvös University Press.
Paulus, E. F. (1982). *Z. Kristallogr.* **160**, 235–243.
Schmidt, M. U., Hofmann, D. W. M., Buchsbaum, C. & Metz, H. J. (2006). *Angew. Chem. Int. Ed* **45**, 1313–1317.
Sheldrick, G. M. (2008). *Acta Cryst.* A**64**, 112–122.
Teteruk, J., Glinnemann, J., Gorelik, T. E., Linden, A. & Schmidt, M. U. (2014). *Acta Cryst.* B**70**, 296–305.
Welberry, T. R. (2004). *Diffuse X-ray Scattering and Models of Disorder.* Oxford University Press.
Welberry, T. R. & Goossens, D. J. (2008). *Acta Cryst.* A**64**, 23–32.
Whitaker, A. (1978). *Z. Kristallogr.* **146**, 173–184.